Emissivity mapping over urban areas using a classification-based approach: Application to the Dual-use European Security IR Experiment (DESIREX)

J.A. Sobrino*, R. Oltra-Carrió, J.C. Jiménez-Muñoz, Y. Julien, G. Sòria, B. Franch, C. Mattar

Global Change Unit, Image Processing Laboratory, University of Valencia, C/Catedrático Agustín Escardino n° 9, 46980 Paterna, Valencia, Spain

ARTICLE INFO

Article history:
Received 14 September 2011
Accepted 17 January 2012

Keywords:
Urban classification
Emissivity maps
Spectral library
TES algorithm
DESIREX

ABSTRACT

In this work a methodology to provide an emissivity map of an urban area is presented. The methodology is applied to the city of Madrid (Spain) using data provided by the Airborne Hyperspectral Scanner (AHS) in 2008. From the data a classification map with twelve different urban materials was created. Each material was then characterized by a different emissivity, whose values were obtained from the application of the TES algorithm to in situ measurements and values extracted from the ASTER spectral library. This new emissivity map could be used as a basis for determining the temperature of the city and to understand the urban heat island effect in terms of spatial distribution and size.

1. Introduction

Remote sensing allows us to obtain a complete picture of all parts of a city and check the behavior of different materials that form the surface at a given time. This method has the advantage of generating urban maps for different applications, e.g. for urban planning or to determine physical parameters such as surface temperature. Finally, from this information we are able to quantify urban phenomena such as the urban heat island (UHI).

The UHI phenomenon refers to the modification of the local climate due to urbanization of the area. The natural surfaces are replaced with artificial ones and, therefore, the thermal properties of materials that cover the surface change. When thermal remote sensing is used to analyze the UHI effect, the term Surface Urban Heat Island (SUHI) is used instead. In this context, Land Surface Temperature (LST) is the parameter being analyzed, because it is the key to understanding the process of energy exchange in the city and directly influences the air temperatures of the layers of the atmosphere next to the surface. Another central surface parameter related to LST is the surface emissivity (ε). Accurate values of LST can be only obtained if surface emissivity is well-characterized, as both parameters are connected by the radiative transfer equation. A variation of 0.01 units in emissivity adds an error of 0.5 °C in the temperature. Therefore the correct retrieval of the emissivity of urban surfaces is of utmost importance because a city is very heterogeneous and its materials have emissivities smaller than 1. Because the emissivity of a material is the relative ability of its surface to emit energy by radiation, it is also important related to the UHI phenomenon or characterization of urban areas in general. As highlighted by Voogt & Oke (2003), very few observations of urban surface emissivity are available, and its retrieval from airborne/satellite imagery is uncertain. Several works have used classification over urban areas to analyze the UHI effect (e.g. Stefanov et al., 2001; Yang et al., 2002; Gluch et al., 2006; Chen et al., 2006; Xian & Crane, 2006; Hartz et al., 2006; Yuan and Bauer, 2007; Imhoff et al., 2010; Myint et al., 2011; etc.). However, only a few works have properly addressed the problem of surface emissivity retrieval over urban areas. Hence, Pu et al. (2006) used a constant value of emissivity for all materials, although the authors stated that it is not well-founded decision to use the same value of ε for all types of surfaces. On the contrary, Kato & Yamaguchi (2005) and Xu et al. (2008) retrieved spectral ε over urban areas in a pixel-by-pixel basis, but little discussion about validity of results was provided.

This paper presents a classification-based approach for spectral surface emissivity mapping over urban areas (particularly over the Madrid city) by combining airborne hyperspectral data, in situ measurements and emissivity spectra included in spectral libraries. The paper has the following sections: Section 2 includes a brief description of the DESIREX field campaign; Section 3 describes the material and methods considered in this study, including description of the study area, airborne imagery, in situ measurements and algorithms used for emissivity retrieval and classification details; Section 4 presents the results obtained in the classification and emissivity retrievals over each urban class, and finally Section 5 includes the main conclusions drawn from this study.

* Corresponding author. Tel.: +34 963 543 115; fax: +34 963 543 261.
E-mail addresses: sobrino@uv.es, jose.sobrino@uv.es (J.A. Sobrino).

2. The Dual-Use European Security IR Experiment: DESIREX-2008

The Dual-use European Security IR Experiment (DESIREX) 2008 was an airborne and ground based campaign of the European Space Agency (ESA) conceived as an experimental campaign in the city of Madrid (Spain) that was carried out in support of the proposed activities for the Reorientation of the Fuegosat Consolidation Phase of the Earth Wathc Programme approved by the ESA in November 2001. The aim of the DESIREX 2008 airborne campaign was to anticipate the generation of thermal datasets to address upcoming trade-off studies supporting both Data User Element (DUE) projects for products prototyping and mission requirements analysis. The "Urban Heat Islands (UHI) and Urban Thermography (UT) Project" was a new Earth Observation Application project funded by DUE within the 3rd Earth Observation Envelope Programme starting on July 2008 that included studies to demonstrate the integration of remote sensing observations in support of UHI mitigation and Urban Energy Efficiency policies. In the framework of the DUE UHI and UT project, ESA organized the dedicated airborne campaign DESIREX 2008 in June and July 2008 in order to generate thermal datasets to be used principally as input to the TIR sensor trade-off study.

The DESIREX 2008 campaign combined the collection of quality and coordinated airborne hyper-spectral, spaceborne and in situ measurements to generate a spectrally, geometrically and radiometrically representative dataset to address observational requirements for UHI and UT monitoring and assessment of an operational system. The period June–July 2008 was chosen to optimize good weather conditions in Madrid. Airborne and satellite imagery and in situ measurements were developed intensively from 23rd June until 6th July 2008. An extensive information about the DESIREX-2008 experiment can be found in Sobrino et al. (2012).

3. Materials and methods

3.1. Study area: Madrid city

Madrid (40° 25′ N, 3° 42′ W, 655 m a.s.l.) is the largest city of Spain (Fig. 1). It is located in a relatively flat area about 50 km south of the Spanish Central Ridge. The main topographic feature is River Manzanares, which crosses the city roughly from west to east. The Manzanares valley causes a small, narrow depression with shoulders rising approximately 75 m to the north and less than 50 m to the south. A secondary feature is a small valley from a tributary stream (Arroyo del Abroñigal) that crosses the city from north to south, joining the Manzanares in the Nudo Sur area of the city. This valley has a depth of 25–30 m. It is important to note that both valleys work frequently as channels for air masses from the cooler northern rural areas. The city districts not affected by the valley slopes are fairly flat, with a gently slope to the north and to the east, so that the maximum city height (at the north of the city) tops roughly to 700 m a.s.l., while the lower occurs in the river Manzanares, around 550 m. Madrid is a large 606 km^2 capital city and with around 3.2 million inhabitants. The area has temperate Mediterranean climate, with cool winters and hot summers. Both these seasons are the dry ones because most of Madrid's rainfall is in the spring and autumn.

3.2. Airborne data

High spatial resolution imagery was acquired with the Airborne Hyperspectral Scanner (AHS), an airborne imaging 80-band

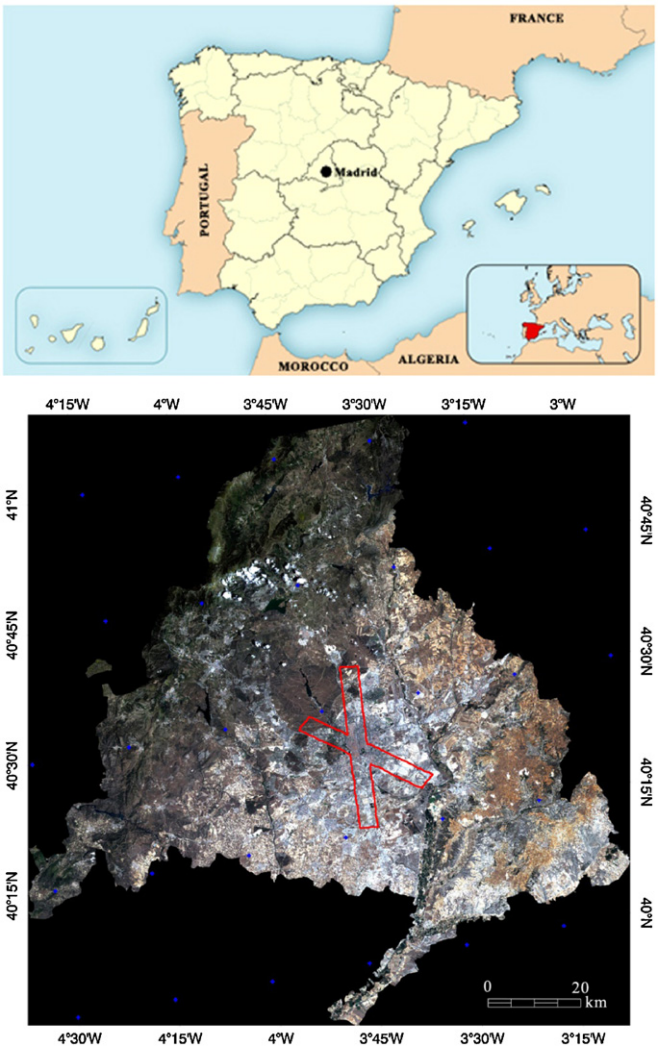

Fig. 1. Location of Madrid city over the Iberian Peninsula and Europe (up) and Madrid province extracted from a Landsat5/TM image with the Airborne Hyperspectral Scanner (AHS) overpasses indicated (bottom).

radiometer developed and built by SensyTech Inc. (currently Argon ST, and formerly Daedalus Ent. Inc.). It contains four types of detectors organized in five optical ports. Port 1 covers the VIS/NIR range from 443 nm up to 1025 nm. In the SWIR range, port 2A has an isolated band centred at 1.6 mm and 990 nm wide. Next, port 2 has a set of continuous narrow bands laying between 1907 nm and 2558 nm. Port 3 covers the MWIR region between 3.1 and 5.5 μm, whereas Port 4 includes 10 bands covering the TIR region between 8.1 and 13.4 μm. Electronic signals coming from the detectors, pre-amplifiers and amplifiers are digitized at 12 bits, and sampled every 2.1 mrad along the FOV (90° = 1.57 rad), that results 750 pixels-samples per scanline. AHS IFOV is 2.5 mrad determined by an square field-stop placed in the middle of its optical path.

A number of AHS flights (daytime and nighttime) were carried out in the DESIREX campaign from 25th of June to 4th of July, 2008, in order to monitor the UHI evolution in the city of Madrid. Two consecutive flights (flight 1, east to west; flight 2, north to south) were acquired each time in order to cover all the representative areas of the city. A description of AHS flights is provided in Table 1. In this paper we considered AHS flights P01I1 and P02I2 (4-July) at near 11:30 GMT, with a pixel size of 4 m (Fig. 2).

Table 1
Description of the AHS flights carried out in DESIREX 2008.

Date (yymmdd)	Time (UTC)	Flight ID	Altitude (m above sea level)	Pixel size (m)
080625	11:11	P01I1	2497	4
080625	11:27	P02I1	2497	4
080625	22:15	P01I2	2497	4
080625	22:31	P02I2	2497	4
080626	04:12	P01ID	2497	4
080626	04:26	P02ID	2497	4
080628	11:32	P01I1	2497	4
080628	11:53	P02I1	2497	4
080628	12:13	P01AD	3409	6
080628	12:31	P02AD	3409	6
080628	20:57	P01BD	1641	2
080628	21:12	P02BD	1641	2
080628	21:29	P01I2	2497	4
080628	21:44	P02I2	2497	4
080701	11:21	P01I1	2497	4
080701	11:44	P02I1	2497	4
080701	21:01	P01BD	1641	2
080701	21:15	P02BD	1641	2
080701	21:29	P01SD	1641	2
080701	21:43	P02SD	1641	2
080701	21:59	P01I2	2497	4
080701	22:12	P02I2	2497	4
080702	04:09	P01ID	2497	4
080702	04:26	P02ID	2497	4
080704	11:16	P01I1	2497	4
080704	11:32	P02I1	2497	4
080704	21.59	P01I2	2497	4
080704	22:14	P02I2	2497	4
080704	22:40	P01AD	3409	6
080704	22:55	P02AD	3409	6

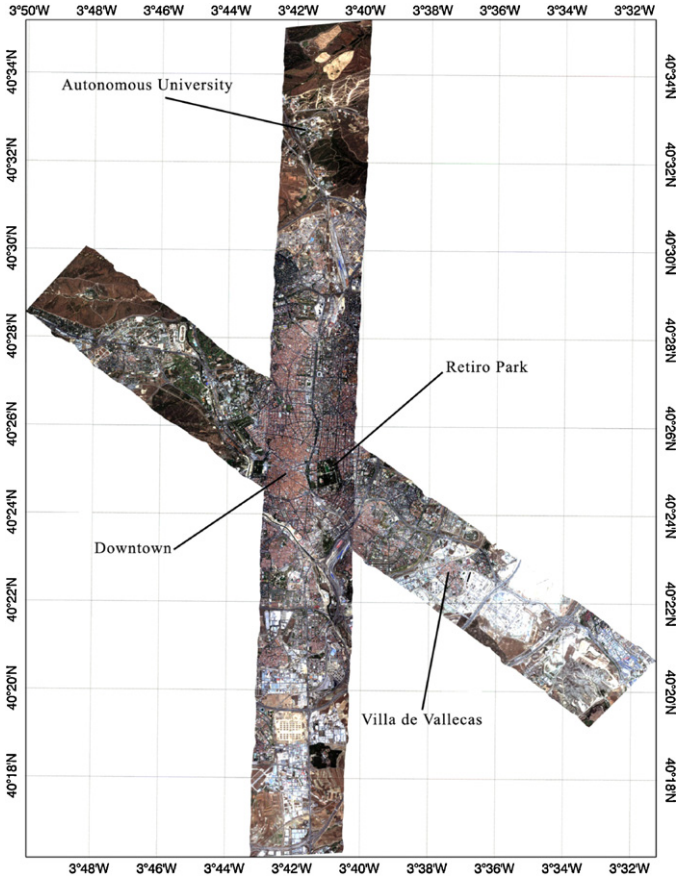

Fig. 2. AHS imagery acquired on 4th July 2008 at around 11:30 GMT over the Madrid city.

Table 2
Spectra of man-made materials included in the ASTER spectral library.

Class	Sub-classes	# samples
Concretes	Construction concretes, paving concretes	5
General construction materials	Bricks, cement cinderblock, cinders, glass, marble, paints, woods	28
Reflectance target	Brass plate, gold plate	27
Road asphalts and tar	Paving asphalts, tar	5
Roofing materials	Metal, roofing paper, rubber, roofing shingle, tile	16

3.3. *In situ measurements*

A complete database of airborne/satellite imagery and in situ measurements was constructed in the framework of the DESIREX-2008 campaign. In situ measurements included atmospheric characterization (radiosoundings, lidar, meteorological stations), surface temperatures using thermal radiometers, air temperature at fixed points and also transects with cars along the city, radiation balance, thermographies, etc. In this paper we will focus on the retrieval of surface emissivity from data measured with multiband thermal radiometers. The instrument used for this purpose was a CIMEL model CE 312-2 ASTER. It has 5 narrow bands (8.13–8.48; 8.48–8.83; 8.93–9.28; 10.25–10.95; 10.95–11.65 μm) and 1 broadband in the spectral region between 8 and 13 μm. It can measure in the range between −80 and 60 °C, with an accuracy of 0.1 °C and a Field of View (FOV) of 10°. Moreover, the sky irradiance has been measured with a diffuse reflectance standard plate (Infragold, Labsphere Inc.). Surface emissivities were retrieved by applying the Temperature and Emissivity Separation (TES) algorithm (see next section) to thermal radiances measured at-ground level.

3.4. *ASTER spectral library*

The ASTER Spectral Library (ASL) is a compilation of more than 2000 spectra covering the region from visible through the region from thermal infrared (0.4–15.4 μm). ASL includes natural and man-made materials and it is available from http://speclib.jpl.nasa.gov. It provides directional hemispherical reflectance values, so emissivity can be obtained via Kirchoff's law, $\varepsilon = 1 - \rho$. Details on sample preparation and sample measurements can be found in Baldridge et al. (2009). In order to analyse the emissivity spectra of urban surfaces, we considered 81 spectra of man-made materials as described in Table 2, and also vegetation (representative of green areas) and water spectra.

3.5. *Surface emissivity retrieval: TES algorithm*

The Temperature and Emissivity Separation (TES) algorithm was originally developed for data collected with the ASTER spaceborne sensor in order to provide to the remote sensing user community with Standard Products of LST and ε. A complete description of the algorithm can be found in Gillespie et al. (1998). The TES algorithm is composed by three modules: NEM (Normalized Emissivity Method), RATIO and MMD (Maximum–Minimum Difference). The NEM module includes an iterative procedure which provides a first guess for LST/ε from atmospherically corrected thermal radiance, sky irradiance and an initial value of ε based on the radiative transfer equation. The RATIO module obtains relative emissivities (called as β-spectrum) by rationing the NEM emissivities to their average value. Finally, the MMD module scales the emissivity spectra in order to provide the final values for LST and ε. The accuracy for the TES algorithm is ±0.015 emissivity units and ±1.5 K. Despite the fact that the method was originally developed for satellite data, it is also

Table 3
Classes defined in the supervised classification obtained from AHS imagery.

Class	Legend
1	Water (lakes)
2	Water (pools)
3	Trees
4	Green grass
5	Bright bare soil
6	Dark bare soil
7	Roads with asphalt
8	Other roads and pavements
9	Roofs with asphalt
10	Roofs with red bricks/tiles
11	Roofs with concrete
12	Roofs with metal
13	Shadows

applicable to ground-based measurements acquired with thermal multiband radiometers (Payan and Royer, 2004; Jiménez-Muñoz & Sobrino, 2006).

The MMD module is the key part of TES algorithm. It relies on an empirical relationship between spectral contrast (MMD) and minimum emissivity (ε_{min}) determined from laboratory and/or field emissivity spectra according to the following expression: $\varepsilon_{min} = a + b \times MMD^c$. Hence, the expression proposed for ASTER data considers the values $a = 0.994$, $b = -0.687$ and $c = 0.737$ based on 86 laboratory spectra of natural surfaces (rocks, soils, vegetation, snow and water), with a regression coefficient $r^2 = 0.983$ and ninety-five percent of the samples falling within ± 0.02 emissivity units. Therefore, it is expected that TES algorithm does not provide satisfactory results over surfaces with ε spectra that do not meet the ε_{min}–MMD relationship. This is the case of surfaces with low spectral contrast (MMD < 0.03), such as water and green vegetation, for which $\varepsilon_{min} = 0.983$ is considered (Gillespie et al., 1998). In Section 4 we will analyse the applicability of the ε_{min}–MMD relationship over man-made materials in order to assess the performance of TES algorithm over urban areas.

3.6. Classification technique

Urban areas have been classified from daytime AHS images using a supervised classification with the Maximum Likelihood as a decision rule. The classes have been defined by taking into account the in situ measurements carried out for the spectral characterization of urban surfaces and also by visual inspection using Google Earth ©. A total amount of 12 classes (plus shadows) were finally selected, as is described in Table 3. An independent dataset of near 200 pixels covering the different classes for each transect were selected to validate the classification results, expressed through the kappa (κ) coefficient. The classification has been performed using at-sensor radiance values (level 1b, in w m^{-2} sr^{-1} μm^{-1}) measured with the four ports (80 spectral bands) of the AHS sensor. The results will be presented in Section 4.

4. Results and discussion

4.1. Classification results

The results obtained in the classification (confusion matrix and kappa coefficient) are provided in Tables 4 and 5 for AHS flights east-west and north-south, respectively. The kappa coefficient is around 70% in both cases. Table 6 provides the percentage of each class included in the two flights. Note that the most abundant classes are "Other roads and pavements" and "Roofs with red bricks/tiles". Minority classes include "Roofs with metal" and "Water". The percentage of vegetation (classes "Trees" and "Green grass") is around 14% for flight P01 and 12% for flight P02, with almost all the vegetation belonging to "Trees" in P01 and equally distributed between "Trees" and "Green grass" in P02. For both flights, water and vegetation classes, which minimize the UHI effect, provide a total percentage of around 15%, whereas the rest of urban areas provide a total percentage higher than 80%. Note that despite this these two flights do not cover the whole urban area of Madrid, they are assumed to be representative samples. Fig. 3 shows respectively the classification maps for flights P01I1 (east-west) and P02I1 (north-south).

It should be noted that other approaches were considered to perform the classification, such as using only at-surface reflectances obtained from the VNIR port data, or using only surface emissivities retrieved from the TIR port data, or even using both at-surface reflectances and emissivities. Other decision rules have also been

Table 4
Confusion matrix and kappa coefficient obtained in the classification of east-west AHS flight. Legend for classes is provided in Table 3.

Classes	1	2	3	4	5	6	7	8	9	10	11	12
1	2	0	0	0	0	0	0	0	0	0	0	0
2	0	3	1	1	0	1	1	0	0	0	0	0
3	0	0	14	1	0	0	0	0	0	0	0	0
4	0	0	0	9	0	0	0	0	0	0	0	0
5	0	0	0	0	4	0	0	5	0	0	0	0
6	0	0	0	0	0	33	0	0	0	0	0	0
7	0	0	1	0	0	0	20	3	0	0	1	0
8	0	0	0	0	13	9	2	28	0	1	4	0
9	0	0	0	0	0	0	0	0	4	0	0	0
10	0	0	1	0	2	1	3	1	2	33	0	0
11	0	0	0	0	0	0	0	3	1	0	3	5
12	0	0	0	0	0	0	0	0	0	0	0	0

Kappa coefficient: 0.73.

Table 5
Confusion matrix and kappa coefficient obtained in the classification of north-south AHS flight. Legend for classes is provided in Table 3.

Classes	1	2	3	4	5	6	7	8	9	10	11	12	13
1	0	0	0	0	0	0	0	0	0	0	0	0	0
2	0	1	2	0	0	0	0	0	0	0	0	0	0
3	0	0	26	1	0	0	0	0	0	0	0	0	0
4	0	0	0	1	0	0	0	0	0	0	0	0	0
5	0	0	0	0	8	0	0	1	0	0	0	0	0
6	0	0	1	0	0	13	0	0	0	0	0	0	0
7	0	0	2	0	0	0	20	2	1	0	1	0	0
8	0	0	5	0	6	10	1	17	0	2	1	0	0
9	0	0	0	0	0	0	3	0	3	0	0	0	0
10	0	0	2	1	0	5	2	2	1	21	2	0	0
11	0	0	0	0	5	5	0	4	1	1	12	1	0
12	0	0	0	0	0	0	0	0	0	0	0	0	0
13	0	0	0	0	0	0	0	0	0	0	0	0	0

Kappa coefficient: 0.67.

Table 6
Percentage of each class included in the AHS flights P01I1 (east-west) and P02I1 (north-south).

Class	Legend	Percentage (%) Flight P01I1	Percentage (%) Flight P02I1
1	Water (lakes)	0.03	0.04
2	Water (pools)	0.88	4.08
3	Trees	12.84	6.77
4	Green grass	1.24	5.48
5	Bright bare soil	6.09	3.05
6	Dark bare soil	8.37	13.02
7	Roads with asphalt	9.58	7.11
8	Other roads and pavements	26.12	30.58
9	Roofs with asphalt	2.53	2.18
10	Roofs with red bricks/tiles	20.09	18.74
11	Roofs with concrete	12.21	7.46
12	Roofs with metal	0.04	1.34
13	Shadows	0	0.15

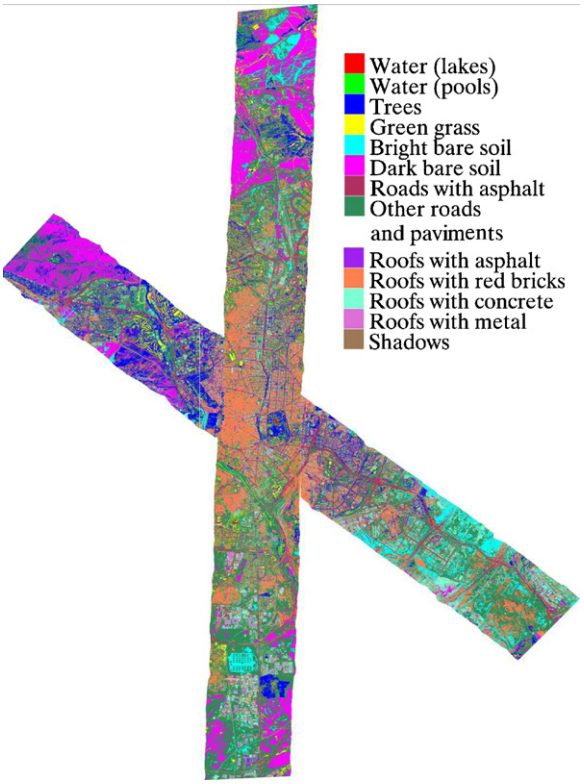

Fig. 3. Classification over the Madrid city using AHS imagery.

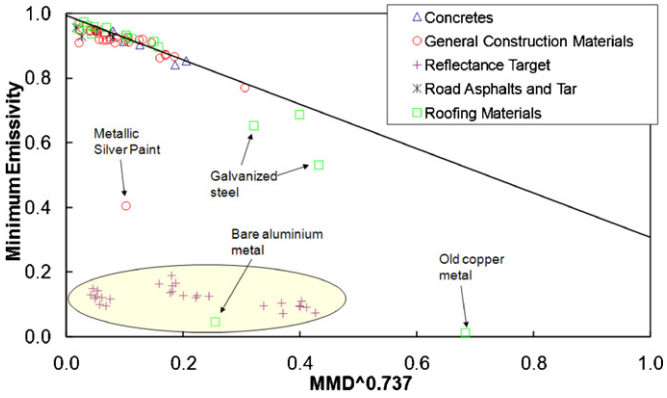

Fig. 4. Plot of minimum emissivity (emin) versus spectral contrast (MMD) for spectra of man-made materials included in the ASTER spectral library. The line given by $\varepsilon_{min} = 0.994 - 0.687\text{MMD}^{0.737}$ (original expression of TES algorithm) is also represented.

tested, such as Linear Discriminant Analysis, Mahalanobis distance, Quadratic Discriminant Analysis and Support Vector Machines. However, these approaches did not significantly improve the resulting κ coefficients. Instead, some urban surfaces have been observed to be better discriminated using surface emissivities, which suggests that a combination of approaches to produce a final classification map could be useful, however, this issue needs further research. Note also that noisy images have been observed for AHS bands 22, 23, 58, 59, 60, 61, 62 and 63. Removal of these bands in the classification procedure did not improve the results significantly.

4.2. Assessment of TES algorithm performance over urban areas

As explained in Section 3.5, TES algorithm relies on the empirical relationship between emin and MMD. In the original TES as presented in Gillespie et al. (1998), this relationship was obtained from spectra of natural surfaces according to $\varepsilon_{min} = 0.994 - 0.687 \times \text{MMD}^{0.737}$. Fig. 4 shows the plot ε_{min} versus MMD of man-made surfaces, in which the line given by the previous expression is also represented. The plot clearly shows that some artificial surfaces do not follow the ε_{min}–MMD relationship, therefore TES algorithm will not provide satisfactory results in these cases. These surfaces include metallic ones (also pointed out by Payan and Royer, 2004) and reference targets, which in fact are made of highly reflectance materials. However there are other methodologies to obtain land surface parameters of these materials, e.g. Malaplate et al. (2001) propose a methodology to retrieve the reflectance of metallic surfaces by using information from 3 μm to 5 μm and alternate measurements under sun and shade. Concretes and asphalts seem to follow the ε_{min}–MMD relationship, therefore valid results are expected when applying the TES algorithm to these surfaces.

4.3. Emissivity maps

Emissivity maps have been elaborated using the classification as a reference, in which emissivity values measured in situ (or extracted from spectral libraries when in situ ones are not available or are expected to be erroneous) have been assigned to each class (Table 7). Because in situ measurements were carried out with the CIMEL CE 312-2 radiometer, with six bands, the emissivity maps obtained from the classification image are referred to these six bands. Note that CIMEL bands from 6 to 2 are equivalent to the five ASTER thermal bands, and CIMEL band 1 is a broadband one between 8 and 13 μm.

Table 7
Emissivity values assigned to each class for the six bands of the CIMEL CE 312-2 radiometer.

Class	Legend	Band6 8.13–8.48 μm	Band5 8.48–8.83 μm	Band4 8.93–9.28 μm	Band3 10.25–10.95 μm	Band2 10.95–11.65 μm	Band1 8–13 μm
1	Water (lakes)[a]	0.983	0.984	0.985	0.990	0.990	0.985
2	Water (pools)[a]	0.983	0.984	0.985	0.990	0.990	0.985
3	Trees[b]	0.990	0.990	0.990	0.990	0.990	0.990
4	Green grass	0.975	0.981	0.980	0.980	0.981	0.978
5	Bright bare soil	0.808	0.802	0.789	0.942	0.956	0.898
6	Dark bare soil[a]	0.962	0.946	0.949	0.941	0.968	0.970
7	Roads with asphalt	0.970	0.977	0.969	0.962	0.964	0.965
8	Other roads and pavements	0.835	0.834	0.817	0.943	0.957	0.914
9	Roofs with asphalt	0.918	0.847	0.775	0.933	0.963	0.897
10	Roofs with red bricks/tiles	0.956	0.911	0.849	0.939	0.942	0.902
11	Roofs with concrete	0.835	0.834	0.817	0.943	0.957	0.914
12	Roofs with metal[a]	0.053	0.053	0.053	0.049	0.046	0.045

[a] Values extracted from the ASTER spectral library.
[b] Constant value assumed taking into account the near-blackbody behavior of vegetation.

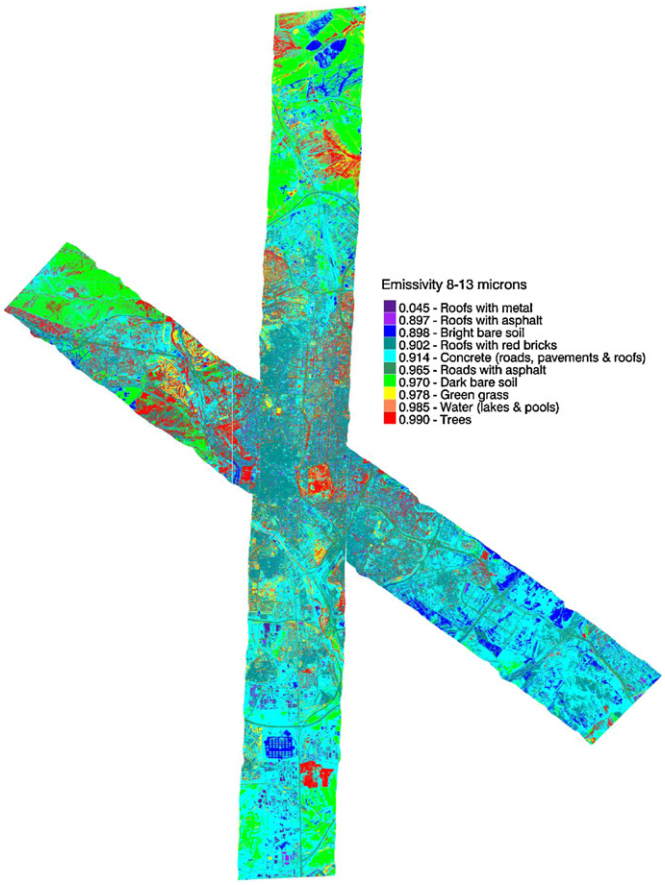

Fig. 5. Emissivity map using the classification-based approach for the broadband ranging between 8 and 13 μm.

As commented in the previous section, the assignation of emissivity values to classes related to urban surfaces is a critical task, some remarks should be pointed out. For example, emissivities for soils are highly variable depending on the soil class. We have adopted the criteria of assigning emissivity values measured at a particular bright soil to the class "bright bare soil", whereas a mean value for soils emissivity extracted from the ASTER spectral library belonging to the *inceptisol* class (the most abundant one in the Earth) has been assigned to the class "dark bare soil". Regarding the retrieval of emissivity values over metallic surfaces, it has been pointed out the TES algorithm fails over this kind of surfaces, because the sky irradiance is almost completely reflected by the surface. Therefore, for the class "Roofs with metal" we have used emissivity spectra for manmade materials included in the ASTER spectral library (class roofing materials – metal). However emissivity for metallic surfaces is also highly variable depending on the material. We have finally selected aluminium as a representative material for metallic roofs. For "vegetated" and "water" areas we have also considered typical emissivity values extracted from the ASTER library. Fig. 5 is an example of the emissivity map obtained from the classification for the broadband (8–13 μm).

In considering the fraction of land covers (Table 6) and the emissivity values assigned to each class for the band 1 (8–13 μm) (Table 7), the total area sensed has an average emissivity of 0.93 for the flight P01I1 and of 0.92 for the flight P02I2. Note that these values of emissivity contribute to an error of 3.5 °C–4 °C in the brightness temperature when the effect of the emissivity is not corrected.

5. Conclusions

As pointed out by different authors, emissivity retrieval over urban areas still remains an open issue. From a remote sensing perspective, surface emissivities should be retrieved from multi- or hyper-spectral TIR data in order to reflect the real condition of the surface. This can be addressed with Temperature and Emissivity Separation algorithms such as the one considered in this paper. However, these algorithms fail over certain kind of surfaces (e.g. metallic ones). The solution proposed in this paper relies on a classification-based approach, in which the TES algorithm is applied to in situ measurements and values are assigned to classes where the algorithm provides satisfactory results, and values extracted from spectral libraries are assigned to the rest of classes. In this last case the selection of the ε-spectra may be somewhat arbitrary, since spectral libraries include "representative" samples but surface over the city can be highly variable in composition and conditions. Research is still needed for development of a TES algorithm applicable to any kind of urban surface.

Acknowledgments

This research was supported by the European Space Agency (DESIREX-20008, project 21717/08/I-LG), European Union (CEOP-AEGIS, project FP7-ENV-2007-1 Proposal No. 212921; WATCH, project 036946) and Ministerio de Ciencia y Tecnología (EODIX, project AYA2008-0595-C04-01). This work has been carried out while R. Oltra-Carrió was in receipt of a grant V Segles from the University of València. The authors thank Dr. Gustavo Camps-Valls (IPL, University of Valencia) for providing classification results using Linear Discriminant Analysis, Mahalanobis distance, Quadratic Discriminant Analysis and Support Vector Machines.

References

Baldridge, A.M., Hook, S.J., Grove, C.I., Rivera, G., 2009. The ASTER spectral library version 2.0. Remote Sensing of Environment 113, 711–715.
Chen, X.-L., Zhao, H.-M., Li, P.-X., Yin, Z.-Y., 2006. Remote Sensing of Environment 104, 133–146.
Gillespie, A., Rokugawa, S., Matsunaga, T., Cothern, J.S., Hook, S., Kahle, A.B., 1998. A temperature and emissivity separation algorithm for advanced spaceborne thermal emission and reflection radiometer (ASTER) images. IEEE Transactions on Geoscience and Remote Sensing 36 (4), 1113–1126.
Gluch, R., Quattrochi, D.A., Luvall, J.C., 2006. A multi-scale approach to urban thermal analysis. Remote Sensing of Environment 104, 123–132.
Hartz, D.A., Prashad, L., Hedquist, B.C., Golden, J., Brazel, A.J., 2006. Linking satellite images and hand-held infrared thermography to observed neighborhood climate conditions. Remote Sensing of Environment 104, 190–200.
Imhoff, M.L., Zhang, P., Wolfe, R.E., Bounoua, L., 2010. Remote sensing of the urban heat island effect across biomes in the continental USA. Remote Sensing of Environment 114, 504–513.
Jiménez-Muñoz, J.C., Sobrino, J.A., 2006. Emissivity spectra obtained from field and laboratory measurements using the temperature and emissivity separation algorithm. Applied Optics 45 (27), 7104–7109.
Kato, S., Yamaguchi, Y., 2005. Analysis of urban heat-island effect using ASTER and ETM+ Data: separation of anthropogenic heat discharge and natural heat radiation from sensible heat flux. Remote Sensing of Environment 99, 44–54.
Malaplate, A., Stoll, M.-P., Nerry, F., 2001. Radiométrie infrarouge Développement et validation de méthodes utilisant la bande [3–5 μm] pour la détermination des paramètres de surface à haute résolution spatiale. PhD Thesis. École Nationale Supérieure de Physique de Strasbourg. Strasbourg: Université Louis Pasteur (Strasbourg I).
Myint, S.W., Gober, P., Brazel, A., Grossman-Clarke, S., Weng, Q., 2011. Per-pixel vs. object-based classification of urban land cover extraction using high spatial resolution imagery. Remote Sensing of Environment, doi:10.1016/j.rse.2010.12.017.
Payan, V., Royer, A., 2004. Analysis of Temperature Emissivity Separation (TES) algorithm applicability and sensitivity. International Journal of Remote Sensing 25 (1), 15–38.
Pu, R., Gong, P., Michishita, R., Sasagawa, T., 2006. Assessment of multi-resolution and multi-sensor data for urban surface temperature retrieval. Remote Sensing of Environment 104, 211–225.

Sobrino, J.A., Oltra-Carrió, R., Sòria, G., Bianchi, R., Paganini, M., 2012. Impact of spatial resolution and satellite overpass time on evaluation of the surface urban heat island effects. Remote Sensing of Environment 117 (0), 50–56.

Stefanov, W.L., Ramsey, M.S., Christensen, P.R., 2001. Monitoring urban land cover change: an expert system approach to land cover classification of semiarid to arid urban centers. Remote Sensing of Environment 77, 173–185.

Voogt, J.A., Oke, T.R., 2003. Thermal remote sensing of urban climates. Remote Sensing of Environment 86, 370–384.

Xian, G., Crane, M., 2006. An analysis of urban thermal characteristics and associated land cover in Tampa Bay and Las Vegas using Landsat satellite data. Remote Sensing of Environment 104, 147–156.

Xu, W., Wooster, M.J., Grimmond, C.S.B., 2008. Modelling of urban sensible heat flux at multiple scales: a demonstration using airborne hyperspectral imagery of Shanghai and a temperature-emissivity separation approach. Remote Sensing of Environment 112, 3493–3510.

Yang, L., Huang, C., Homer, C., Wylie, B., Coan, M., 2002. An approach for mapping large-area impervious surfaces: synergistic use of Landsat 7 ETM+ and high spatial resolution imagery. Canadian Journal of Remote Sensing 29 (2), 230–240.

Yuan, F., Bauer, M.E., 2007. Comparison of impervious surface area and normalized difference vegetation index as indicators of surface urban heat island effects in Landsat imagery. Remote Sensing of Environment 106, 375–386.